

Gate-tunable Intrinsic Anomalous Hall Effect in Epitaxial MnBi₂Te₄ Films

Shanshan Liu,^{1,2#} Jiexiang Yu,^{3#} Enze Zhang,¹ Zihan Li,^{1,2} Qiang Sun⁴, Yong Zhang,⁵ Lun Li,⁵ Minhao Zhao,^{1,2} Pengliang Leng,^{1,2} Xiangyu Cao,^{1,2} Jin Zou,^{4,6} Xufeng Kou,⁵ Jiadong Zang,⁷ Faxian Xiu^{1,2,8,9*}

¹State Key Laboratory of Surface Physics and Department of Physics, Fudan University, Shanghai 200433, China

²Shanghai Qi Zhi Institute, 41th Floor, AI Tower, No. 701 Yunjin Road, Xuhui District, Shanghai 200232, China

³School of Physical Science and Technology, Soochow University, Suzhou 215006, China

⁴Materials Engineering, The University of Queensland, Brisbane QLD 4072, Australia

⁵School of Information Science and Technology, ShanghaiTech University, Shanghai 201210, China

⁶Centre for Microscopy and Microanalysis, The University of Queensland, Brisbane QLD 4072, Australia

⁷Department of Physics and Astronomy, University of New Hampshire, Durham, New Hampshire 03824, USA.

⁸Institute for Nanoelectronic Devices and Quantum Computing, Fudan University, Shanghai 200433, China

⁹Shanghai Research Center for Quantum Sciences, Shanghai 201315, China

These authors contributed equally to this work

*Correspondence and requests for materials should be addressed to F. X. (Email: Faxian@fudan.edu.cn).

Anomalous Hall effect (AHE) is an important transport signature revealing topological properties of magnetic materials and their spin textures. Recently, antiferromagnetic MnBi₂Te₄ has been demonstrated to be an intrinsic magnetic topological insulator that exhibits quantum AHE in exfoliated nanoflakes. However, its complicated AHE behaviors may offer an opportunity for the unexplored correlation between magnetism and band structure. Here, we show the Berry curvature dominated intrinsic AHE in wafer-scale MnBi₂Te₄ thin films. By utilizing a high-dielectric SrTiO₃ as the back-gate, we unveil an ambipolar conduction and electron-hole carrier (*n-p*) transition in ~7 septuple layer MnBi₂Te₄. A quadratic relation between the saturated AHE resistance and longitudinal resistance suggests its intrinsic AHE mechanism. For ~3 septuple layer MnBi₂Te₄, however, the AHE reverses its sign from pristine negative to positive under the electric-gating. The first-principles calculations demonstrate that such behavior is due to the competing Berry curvature between polarized spin-minority-dominated surface states and spin-majority-dominated inner-bands. Our results shed light on the physical mechanism of the gate-tunable intrinsic AHE in MnBi₂Te₄ thin films and provide a feasible approach to engineering its AHE.

Introduction

The study of anomalous Hall effect (AHE) is fundamental yet critical for understanding electron properties and magnetic couplings in magnetic materials^{1,2}. In contrast to the normal Hall effect induced by Lorentz force, the AHE in magnetic compounds, especially with the ferromagnetism, correlates with the crystal structure and spin-orbit coupling^{1,3,4}. There are three established microscopic mechanisms. Momentum-space Berry curvature contributes to the intrinsic AHE that depends on band structures⁵. Side jump and skew-scattering, resulted from opposite electron deflection and asymmetric electron scattering when approaching impurities⁶⁻⁸, constitute the extrinsic effects of AHE. Through tracking the AHE evolution, the interaction between carriers and spins was discovered in traditional diluted magnetic semiconductors (In, Mn)As⁹. Magnetic exchange interaction was also found to switch from the Ruderman-Kittel-Kasuya-Yoshida (RKKY) to the Van-Vleck effect owing to the enhanced direct magnetic coupling of local electrons in heavily-doped ferromagnetic films¹⁰. Recently, the AHE has been extended to the antiferromagnetic compounds with unique magnetic textures or band structures, for example, the large AHE in the noncollinear Mn₃Sn antiferromagnet¹¹. In topological semimetal antiferromagnetic RPtBi (R is a rare earth element), the AHE is originated from the large Berry curvature introduced by Weyl points and magnetic textures^{12,13}.

When combining topological insulators with magnetism, a new topological phase, magnetic topological insulators can be developed which hold a surface exchange gap induced by a long-range ferromagnetic order. Many exotic phenomena were predicted in magnetic topological insulators, for instance, the quantum anomalous Hall effect and magnetic monopoles¹⁴⁻¹⁶. Through doping magnetic atoms into topological insulators, quantum anomalous Hall effect and topological Hall effect were detected¹⁷⁻²¹. Also, by employing magnetic insulators as the substrate, topological insulators with perpendicular ferromagnetism can be constructed due to the interfacial proximity effect²²⁻²⁴. However, disorders induced by the doping or lattice mismatch are almost inevitable, and films with high uniformity and stable magnetism are highly pursued^{20,25,26}. Meanwhile, searching for intrinsic magnetic topological insulators with pristine magnetism and topological band structure becomes indispensable. To date, MnBi₂Te₄ has been experimentally confirmed to be an intrinsic magnetic topological insulator²⁷⁻²⁹. Due to the A-type antiferromagnetic order, versatile quantum properties in odd/even layers have been detected³⁰⁻³⁵. However, these findings in MnBi₂Te₄ flakes are susceptible to other extrinsic factors, like sample quality, suggesting that disorders and magnetization can significantly tune the electronic properties. Moreover, MnBi₂Te₄ in bulk crystals and exfoliated flakes were extensively studied with rare films involved which show complex AHE behaviors³⁶⁻³⁸. How the band structure correlates with the AHE and what kind of magnetism coupling exist, RKKY or Van-Vleck effect, pose open questions in MnBi₂Te₄.

Here, we report the gate-tunable Berry-curvature-dominated anomalous Hall effect in MnBi₂Te₄ films. Wafer-scale high crystalline MnBi₂Te₄ thin films have been directly deposited on (001) Al₂O₃ and (111) SrTiO₃ substrates. The antiferromagnetism, perpendicular magnetic anisotropy, and anomalous Hall insulator state of MnBi₂Te₄ thin films are demonstrated. By

controlling the gate voltage, we have witnessed the electron-hole carrier (n - p) transition in the ~ 7 septuple layer (SL) sample and the reversed AHE sign in the ~ 3 SL sample. The intrinsic AHE is confirmed to be irrelevant to the carrier type or density. Band structure and Berry curvature calculations find that as the Fermi energy increases, the main conduction band switches from spin-minority to spin-majority bands, and the anomalous Hall conductivity changes from positive to negative. Our first-principles calculations explain the experimental finding and map the gated Fermi energy within the band structure.

Results

Layered tetradymite MnBi_2Te_4 is a trigonal structure with $\text{Te}^{2-}\text{-Bi}^{3+}\text{-Te}^{2-}\text{-Mn}^{2+}\text{-Te}^{2-}\text{-Bi}^{3+}\text{-Te}^{2-}$ septuple layer like MnTe bilayer intercalated into Bi_2Te_3 quintuple layer, as schematically depicted in Fig. 1a. The A-type antiferromagnetic (AF) order on Mn can be described as intralayer ferromagnetic (FM) and interlayer AF coupling, as marked by green arrows. We successfully synthesized 2-inch high-quality MnBi_2Te_4 films on (001) Al_2O_3 and (111) SrTiO_3 substrates using molecular beam epitaxy by co-evaporating three elements of Mn, Bi, and Te (Fig. 1b inset) and by adjusting the element flux ratio and substrate temperature. The oscillation of the reflection-high-energy-electron-diffraction (RHEED) intensity during the growth of a 14 SL film on Al_2O_3 is shown in Fig. 1b, with a composition of $\text{MnBi}_{2.03}\text{Te}_{3.94}$ (Fig. S2a). The layer-by-layer growth mode is verified via periodic oscillations with a growth rate of 310 s/layer. The upper right inset of Fig. 1b shows a streaky RHEED diffraction pattern, suggesting a smooth surface. In Fig. 1c, the layered structure is further characterized by cross-section high-resolution transmission electron microscopy (HRTEM) and the layer distance is about 1.39 nm. The corresponding selected-area-electron-diffraction (SAED) results further identify the single-crystallinity (Fig. 1d). The epitaxial orientation of $\{003\}$ is also confirmed by X-ray diffraction (XRD), as shown in Fig. 1e. Note that due to the thickness of 14 SL, signals from Al_2O_3 can also be captured in XRD and SAED measurements. The lattice constants of the thin film are $a=4.38$ Å and $c=40.71$ Å, consistent with the bulk values³⁹. The detailed structural analysis is provided in Supplementary Section 1. We further conducted the magnetization measurements of zero-field-cooled (ZFC) and field-cooled (FC) magnetization and field-dependent magnetization to explore its magnetic properties. As illustrated in Fig. 1f, our 34 SL MnBi_2Te_4 film possesses the AF characteristic with a Néel temperature (T_N) of ~ 25.2 K, close to the bulk value^{40,41}. Multiple steps in M - H hysteresis further confirm its antiferromagnetic property (Fig. 1f inset). As the magnetic field increases above 5 T, spins of Mn are aligned along the field direction and the spin-polarized state can be generated. Employing the experimental lattice constants, the density functional theory (DFT) calculations for MnBi_2Te_4 bulk show that the A-type AF state is 1.5 meV per Mn lower in energy than the FM state, confirming the experimental observation.

To investigate transport properties, we carried out magneto-transport measurements on $\text{MnBi}_2\text{Te}_4/\text{Al}_2\text{O}_3$ films to measure four-terminal longitudinal resistance (R_{xx}) and anomalous Hall resistance (R_{xy}^A). We subtracted the linear component of the normal Hall resistance (R_{xy}^H). Figure 2a shows the R_{xx} of a 9 SL film. R_{xx} rises with temperature dropping so it behaves

as an insulator. A phase transition temperature appears at 19.8 K and corresponds to its Néel temperature T_N . Due to the enlarged thermal fluctuation effect in thin films, T_N is smaller than the bulk value^{40,41}. The activation energy E_a is about 9.6 meV by fitting R_{xx} at high temperatures to $R_{xx} \sim \exp(E_a/k_B T)$ where k_B is the Boltzmann constant. The band gap (E_{gap}) is roughly estimated to be larger than 19.2 meV. Angle-dependent AHE under 1.5 K is shown in Fig. 2b, with the angle (θ) defined as the angle between the magnetic field and the normal orientation of the sample surface. Perpendicular magnetic anisotropy can be validated as the saturation field (H_s) rises monotonously with the increasing angle. It was later confirmed by the DFT calculations that the perpendicular geometry of the A-type AF order is 0.8 meV per Mn lower in energy than the in-plane spin directions. Because of the A-type AF order with weak interlayer coupling, Mn from different layers can flip their spins independently so the multiple magnetic intermediate spin-flop states with kinks are identified in the R_{xy}^A curve. In the temperature-dependent AHE measurement with $\theta=0^\circ$, both R_{xy}^A and coercive field (H_c) decrease monotonously as the temperature rises. The saturated anomalous Hall resistance (R_{xy}^{AS}) is about 6.72 k Ω (1.5 K).

The thickness-dependent AHE is obtained for 7 SL to 14 SL MnBi₂Te₄/Al₂O₃, as shown in Fig. 2d. R_{xy}^A as well as the hysteresis window decreases monotonously as the thickness increases. It is attributed to the larger magnetic anisotropy in thinner samples which have been reported in two-dimensional ferromagnetic materials^{42,43}. To make this clear, the extracted temperature-dependent coercive field (H_c) is drawn in Fig. 2d inset. As the film becomes thicker, more spin-flop states (in some cases, degenerate) can be generated, and the differences between each adjacent spin-flop state become smaller (Fig. 2d). It is reported that the quantum anomalous Hall effect with nearly quantized R_{xy}^A and quenched R_{xx} can be observed in low-disorder co-doped topological insulators⁴⁴ (named as quantum anomalous Hall insulator). At the same time, the decreased R_{xy}^A and increased R_{xx} can also appear due to the increased magnetic disorder (denoted as anomalous Hall insulator). Such behaviors can be analyzed via the evolution of R_{xx} . Zero-field R_{xx} (R_{xx}^0) and R_{xx} at H_c ($R_{xx}^{H_c}$) of different MnBi₂Te₄ films from 7 SL to 14 SL exhibit a positive trend (Fig. 2e) and indicates that the MnBi₂Te₄ films share the anomalous Hall insulator state with strong local magnetic disorder although the high crystallinity has been proved by structural characterizations.

We further investigated the AHE with the modulation of the Fermi-level to connect it with the band structure. A high dielectric SrTiO₃ is served as the back-gate and two MnBi₂Te₄ samples were synthesized on 0.25 mm-thick (111) SrTiO₃ substrates and fabricated into a six Hall-bar structure (Fig. 3c). The thickness of the two samples is 5 nm and 10 nm, estimated to be ~ 3 SL and ~ 7 SL, respectively. Both the pristine samples show the electron-dominated semiconducting properties (n -type, see Figs. S5 and S8). Let's first analyze the ~ 7 SL film. Figure 3a shows the representative Hall resistance R_{xy} curves at different gate voltages (V_g), and the corresponding R_{xy}^A results (Fig. 3b) are obtained by subtracting the linear component from the normal Hall effect. In the positive V_g , the negative slopes of R_{xy} curves indicate the n -type conduction but the negative V_g flips the sign of the slope, indicating hole-carrier (p -

type) conduction. This electron-hole (n - p) transition suggests that the Fermi-level is moved from the conduction band to the valence band as V_g decreases (Fig. 3d inset). The normal Hall resistance $R_{xy}^H = R_H B$ is proportional to the magnetic field B , so the sheet carrier density at each gate voltage can be extracted by $1/(R_H \cdot e)$ where e is the elementary charge, as shown in Fig. 3d. With V_g decreasing, the electron density shows a dramatically declining behavior while the hole density does not change much. Secondly, the hole density is larger than the electron density near the n - p transition. These findings indicate a narrow conduction band and a broad valence band, as schematically shown in Fig. 3d inset. To avoid the large errors of the estimated carrier density because of the complex Hall slope, we do not extract the carrier density near the critical n - p transition regime. The critical n - p transition regime is also verified by the longitudinal resistance R_{xx}^0 processed by the symmetric methods³⁰, as shown in Fig. 3e. R_{xx}^0 has an ambipolar behavior with a maximum of 13.86 k Ω at $V_g = 10$ V, and the asymmetric feature demonstrates the different properties between electron and hole carriers. We note that the carrier conduction switches from electrons to holes and the carrier density changes (Fig. 3d). The negative sign of R_{xy}^A is preserved in the whole measurement. The small kink at about ± 3 T corresponds to the magnetic transition. The R_{xy}^{AS} also shows an ambipolar feature with a maximum of 844 Ω at $V_g = 20$ V. The relation between R_{xy}^{AS} and R_{xx}^0 in both electron and hole regions follow the quadratic scaling of $R_{xy}^{AS} \propto (R_{xx}^0)^2$ (Fig. 3f). It thus gives a strong support for the intrinsic AHE dominated by Berry curvature in MnBi₂Te₄ films.

Distinct from the n - p transition in ~ 7 SL device, R_{xy} of ~ 3 SL film behaves n -type conduction in the whole V_g range of ± 160 V, and the field-dependent R_{xy} and the corresponding R_{xy}^A curves at various gate voltages are illustrated in Figs. 4a and 4b, respectively. However, in contrast to the ~ 7 SL sample, R_{xy}^{AS} in ~ 3 SL changes its sign at positive V_g where R_{xy}^{AS} is positive/negative under the positive/negative saturated magnetic field (Fig. 4b). We call respectively positive- and negative-sign AHE when R_{xy}^{AS} has the same and opposite sign with the saturated magnetic field. With various V_g , the saturated R_{xy}^{AS} and the corresponding R_{xx}^0 are shown in Fig. 4c. The AHE polarity switches its sign at $V_g = 30$ V. The magnitudes of positive-sign AHE are much smaller than those of negative-sign AHE. R_{xx}^0 increases monotonously as V_g scans from positive to negative. It indicates that the carrier density decreases as V_g reduces, consistent with the evolution of n_s extracted from the linear Hall slope (Fig. S8d). The quadratic relations $R_{xy}^{AS} \propto (R_{xx}^0)^2$ between R_{xy}^{AS} and R_{xx}^0 are also verified for both positive- and negative-sign AHE, as shown in Fig. 4d, confirming the Berry curvature dominated intrinsic AHE. To check the magnetic tunability, we have exploited the temperature-dependent R_{xy} under different gating voltages. We found that MnBi₂Te₄ films contain pristine and stable magnetism under different V_g , with the T_N nearly unchanged irrespective of the carrier type and density (Supplementary Figs. S7, S10).

Due to the antiferromagnetic order, the even layer MnBi₂Te₄ always brings about zero AHE. Thus, by using first-principles calculations with the assistance of the maximally-localized Wannier functions method, the band structures and their corresponding intrinsic

anomalous Hall conductivity σ_{xy}^A were calculated for 3, 5, and 7 SL MnBi₂Te₄. Under the perpendicular antiferromagnetic spin order where the spins at the first and the last layer are set to be the up direction, the band structures are shown in Fig. 5a-c. For all three films, a bandgap of about 0.05 eV appears at the Fermi energy with the insulating nature, consistent with the activated energy E_a . The corresponding anomalous Hall conductivities with various Fermi energies are summarized in Fig. 5d. Inside the bandgap, the non-zero platform of σ_{xy}^A appears for all three films. The magnitude of the platform is exactly e^2/h , indicating the quantum anomalous Hall effect. Above the gap, σ_{xy}^A decays significantly as the Fermi energy increases. Valence bands are narrower than conduction bands so it confirms the carrier density results in Fig. 3d.

The experimental σ_{xy}^A is obtained by using the equation $\sigma_{xy}^A = \rho_{xy}^A / (\rho_{xx}^2 + \rho_{xy}^{A2})$ in Fig. 5e. The experimental σ_{xy}^A with all gate voltages are far from e^2/h . Since the ratio of (Mn, Bi, Te) in our MnBi₂Te₄ is not perfect (1, 2, 4), it might be caused by the defects of the thin films, magnetic disorders from impurities, or the effect by the substrate. However, a peak of about 10 S/cm appears at $V_g = 30$ V for ~ 7 SL film. Because the n - p transition also happens around that gate voltage, we can deduce that the peak position corresponds to the bandgap. In ~ 3 SL, σ_{xy}^A is even one order of magnitude smaller than that in ~ 7 SL. Moreover, σ_{xy}^A changes its sign around $V_g = 30$ V. According to the theoretical σ_{xy}^A for 3 SL in Fig. 5d, there is also a sign transition of σ_{xy}^A around $E_F = 0.12$ eV. The reason for the sign transition is in the following. For all three calculated films (Figs. 5a-c), the first two conduction bands are dominated by spin minority or spin-down component that corresponds to the two surface states (ss) of the films. The spin-down dominated conduction bands lead to the negative-sign AHE. Around 0.1~0.15 eV above the Fermi energy, one band for 3 SL, three bands for 5 SL, and five bands for 7 SL correspond to bands of inner-layers and they are dominated by spin majority or spin up component. The change of the spin component at the Fermi energy (see spin polarization in Fig. S15) leads to the sign change of σ_{xy} . Therefore, $V_g = 30$ V of ~ 3 SL film is mapped to $E_F = 0.12$ eV of 3 SL (Fig. 5a). The mapping from the gate voltage of ~ 3 SL and ~ 7 SL to the Fermi energy of 3 SL and 7 SL are labeled, respectively, as shown in Figs. 5a and c. While in ~ 3 SL film, gating leads to all n -type conduction, gating in ~ 7 SL sample, however, crosses the bandgap and causes the n - p transition.

Conclusion

In summary, by precisely controlling the flux ratios, wafer-scale high-crystalline MnBi₂Te₄ films have been directly deposited on Al₂O₃ and SrTiO₃ substrates by the co-evaporation process. We demonstrate the antiferromagnetism, perpendicular magnetic anisotropy, and anomalous Hall insulator state via temperature- and thickness-dependent AHE analysis. Our further study on the gating control of SrTiO₃-substrated samples identifies the n - p transition and ambipolar transport in ~ 7 SL films and the sign-reversal behavior of AHE in ~ 3 SL films. Both display quadratic relations of R_{xy}^{AS} and R_{xx}^0 , indicating the intrinsic Berry-curvature-induced AHE. The band structure and Berry curvature calculations show that the

anomalous Hall conductivities qualitatively match the experimental values. We also attribute the sign reversal of AHE to the competing Berry curvature between polarized spin-minority-dominated surface states and spin-majority-dominated inner-bands. In addition, the mapping from the gate voltages to the Fermi levels of the band structures is provided. Our study provides the synthesis of complex materials and presents an approach to control AHE, which may facilitate the exploration of new physical mechanisms.

Methods

Thin-film synthesis and characterization

MnBi₂Te₄ films were grown on (001) Al₂O₃ and (111) SrTiO₃ substrates in Perkin Elmer 430 MBE with the *in-situ* RHEED facility. Al₂O₃ and SrTiO₃ substrates were initially degassed at 600 °C and 500 °C for half an hour respectively and then decreased to the aimed temperature for the growth. Mn (99.99%), Bi (99.999%), and Te (99.9999%) three elements were co-evaporated from Knudsen cells with the source temperature of 686 °C, 460°C, and 287 °C, respectively. The flux of each element was calibrated by the crystal monitor. Before taking samples out of the chamber, 2 nm Al were capped for protection. The structural characteristics were studied by XRD (Bruker D8 Discover) and TEM (FEI Tecnai F20). The cross-section TEM sample was prepared using FIB (FEI Scios DualBeam). The films' thickness on SrTiO₃ was measured by AFM (Park NX10) as the substrates were too small to be directly monitored by *in-situ* RHEED during the growth.

Electrical and magnetization measurement

For the magneto-transport experiment, thin films were cut and confined to the six Hall-bar structures and measured by Physical Properties Measurement System (PPMS, 9 T) and Oxford System (TeslatronPT, 12 T), with data collected by SR830 and Agilent B2912A. The magnetization measurements were performed in DC-Superconducting-Quantum-Interface-Devices (SQUID, 7 T).

Band structure calculations

Total energies and electronic structures of MnBi₂Te₄ bulk and thin films were calculated from first-principles calculations within the framework of density functional theory using the projector augmented wave pseudopotential^{45,46} as implemented in VASP^{47,48}. The generalized gradient approximation of Perdew, Burke, and Ernzerhof⁴⁹ was used for the exchange-correlation energy, and the Hubbard U method⁵⁰ with $U = 4.0$ eV and $J = 0.9$ eV was applied on the Mn($3d$) orbitals. An energy cutoff of 600 eV for the plane-wave expansion was used. Non-collinear magnetism calculations with spin-orbit coupling included were employed. The Γ -centered k -point mesh of $9 \times 9 \times 9$, $7 \times 7 \times 7$, and $9 \times 9 \times 1$ in the Brillouin zone (BZ) was adopted for the calculations of trigonal ferromagnetic bulk, trigonal antiferromagnetic bulk and thin-film structures by using a supercell slab with a 13.57Å vacuum layer along z direction, respectively. After we obtained the eigenstates and eigenvalues, a unitary transformation of Bloch waves was performed to construct the tight-binding Hamiltonian in a Wannier function (WF) basis by using the maximally-localized Wannier functions method⁵¹ implemented in the

Wannier90 package⁵². WF-based Hamiltonian has the same eigenvalues as those obtained by first-principles calculations from -1.0 ~ 1.0 eV to the Fermi level. The intrinsic anomalous Hall conductivity for thin films was calculated using the WF-based Hamiltonian based on Berry curvature with a 640×640 k-mesh in two-dimensional BZ.

Acknowledgments

This work was supported by the National Natural Science Foundation of China (11934005 and 11874116), the National Key Research and Development Program of China (Grant No. 2017YFA0303302 and 2018YFA0305601), the Science and Technology Commission of Shanghai (Grant No. 19511120500), the Shanghai Municipal Science and Technology Major Project (Grant No. 2019SHZDZX01), the Program of Shanghai Academic/Technology Research Leader (Grant No. 20XD1400200). E.Z. acknowledges support from China Postdoctoral Innovative Talents Support Program (Grant No. BX20190085) and China Postdoctoral Science Foundation (Grant No. 2019M661331). S.L. acknowledges support from China Postdoctoral Science Foundation (Grant No. 2020TQ0080 and 2020M681138). We acknowledge Zhengcai Xia and Jinglei Zhang for assistance in high-field experiments.

Author contributions

F.X. conceived the ideas and supervised the overall research. S.L. and Z.L. synthesized the MnBi_2Te_4 films and measured the XRD. S.L., E.Z., Y.Z. L.L. M.Z., P.L., X.C. and X.K. performed the magneto-transport measurement and analyzed the data. S.L. and E.Z. carried out the SQUID measurement and analyzed the results. Q.S. and J.Z. did the TEM characterization. J.Y. and J.Z. performed the DFT calculations and the theoretical analyses. S.L., J.Y. and F.X. wrote the paper with assistance from all other authors.

Competing financial interests

The authors declare no competing financial interests.

Data availability

The data that support the plots within this paper and other findings of this study are available from the corresponding author upon reasonable request.

Reference

1. Nagaosa, N., Sinova, J., Onoda, S., MacDonald, A. H. & Ong, N. P. Anomalous Hall effect. *Rev. Mod. Phys.* **82**, 1539–1592 (2010).
2. Sinitsyn, N. A. Semiclassical theories of the anomalous Hall effect. *J. Phys. Condens. Matter* **20**, 023201 (2007).
3. Ghimire, N. J. *et al.* Large anomalous Hall effect in the chiral-lattice antiferromagnet CoNb_3S_6 . *Nat. Commun.* **9**, 3280 (2018).
4. Chen, H., Niu, Q. & MacDonald, A. H. Anomalous Hall Effect Arising from Noncollinear Antiferromagnetism. *Phys. Rev. Lett.* **112**, 017205 (2014).

5. Karplus, R. & Luttinger, J. M. Hall Effect in Ferromagnetics. *Phys. Rev.* **95**, 1154–1160 (1954).
6. Berger, L. Side-Jump Mechanism for the Hall Effect of Ferromagnets. *Phys. Rev. B* **2**, 4559–4566 (1970).
7. Smit, J. The spontaneous hall effect in ferromagnetics I. *Physica* **21**, 877–887 (1955).
8. Smit, J. The spontaneous hall effect in ferromagnetics II. *Physica* **24**, 39–51 (1958).
9. Ohno, H., Munekata, H., Penney, T., von Molnár, S. & Chang, L. L. Magnetotransport properties of p-type (In,Mn)As diluted magnetic III-V semiconductors. *Phys. Rev. Lett.* **68**, 2664–2667 (1992).
10. Kou, X. *et al.* Interplay between Different Magnetisms in Cr-Doped Topological Insulators. *ACS Nano* **7**, 9205–9212 (2013).
11. Nakatsuji, S., Kiyohara, N. & Higo, T. Large anomalous Hall effect in a non-collinear antiferromagnet at room temperature. *Nature* **527**, 212–215 (2015).
12. Suzuki, T. *et al.* Large anomalous Hall effect in a half-Heusler antiferromagnet. *Nat. Phys.* **12**, 1119 (2016).
13. Zhu, Y. *et al.* Exceptionally large anomalous Hall effect due to anticrossing of spin-split bands in the antiferromagnetic half-Heusler compound TbPtBi. *Phys. Rev. B* **101**, 161105 (2020).
14. Hasan, M. Z. & Kane, C. L. Colloquium: Topological insulators. *Rev. Mod. Phys.* **82**, 3045–3067 (2010).
15. Haldane, F. D. M. Model for a Quantum Hall Effect without Landau Levels: Condensed-Matter Realization of the ‘Parity Anomaly’. *Phys. Rev. Lett.* **61**, 2015–2018 (1988).
16. Tokura, Y., Yasuda, K. & Tsukazaki, A. Magnetic topological insulators. *Nat. Rev. Phys.* **1**, 126–143 (2019).
17. Liu, N., Teng, J. & Li, Y. Two-component anomalous Hall effect in a magnetically doped topological insulator. *Nat. Commun.* **9**, 1282 (2018).
18. Chang, C.-Z. *et al.* Experimental Observation of the Quantum Anomalous Hall Effect in a Magnetic Topological Insulator. *Science* **340**, 167–170 (2013).
19. Chang, C.-Z. *et al.* High-precision realization of robust quantum anomalous Hall state in a hard ferromagnetic topological insulator. *Nat. Mater.* **14**, 473–477 (2015).
20. Ou, Y. *et al.* Enhancing the Quantum Anomalous Hall Effect by Magnetic Codoping in a Topological Insulator. *Adv. Mater.* **30**, 1703062 (2018).
21. Liu, C. *et al.* Dimensional Crossover-Induced Topological Hall Effect in a Magnetic Topological Insulator. *Phys. Rev. Lett.* **119**, (2017).
22. Wei, P. *et al.* Exchange-Coupling-Induced Symmetry Breaking in Topological Insulators. *Phys. Rev. Lett.* **110**, 186807 (2013).
23. Lang, M. *et al.* Proximity Induced High-Temperature Magnetic Order in Topological Insulator - Ferrimagnetic Insulator Heterostructure. *Nano Lett.* **14**, 3459–3465 (2014).
24. Alegria, L. D. *et al.* Large anomalous Hall effect in ferromagnetic insulator-topological insulator heterostructures. *Appl. Phys. Lett.* **105**, 053512 (2014).
25. Feng, X. *et al.* Thickness Dependence of the Quantum Anomalous Hall Effect in Magnetic

- Topological Insulator Films. *Adv. Mater.* **28**, 6386–6390 (2016).
26. Lee, I. *et al.* Imaging Dirac-mass disorder from magnetic dopant atoms in the ferromagnetic topological insulator $\text{Cr}_x(\text{Bi}_{0.1}\text{Sb}_{0.9})_{2-x}\text{Te}_3$. *Proc. Natl. Acad. Sci.* **112**, 1316–1321 (2015).
 27. Otrokov, M. M. *et al.* Prediction and observation of an antiferromagnetic topological insulator. *Nature* **576**, 416–422 (2019).
 28. Li, J. *et al.* Intrinsic magnetic topological insulators in van der Waals layered MnBi_2Te_4 -family materials. *Sci. Adv.* **5**, eaaw5685 (2019).
 29. Zhang, D. *et al.* Topological Axion States in the Magnetic Insulator MnBi_2Te_4 with the Quantized Magnetoelectric Effect. *Phys. Rev. Lett.* **122**, 206401 (2019).
 30. Deng, Y. *et al.* Quantum anomalous Hall effect in intrinsic magnetic topological insulator MnBi_2Te_4 . *Science* **367**, 895–900 (2020).
 31. Liu, C. *et al.* Robust axion insulator and Chern insulator phases in a two-dimensional antiferromagnetic topological insulator. *Nat. Mater.* **19**, 522–527 (2020).
 32. Ge, J. *et al.* High-Chern-number and high-temperature quantum Hall effect without Landau levels. *Natl. Sci. Rev.* **7**, 1280–1287 (2020).
 33. Yang, S. *et al.* Odd-Even Layer-Number Effect and Layer-Dependent Magnetic Phase Diagrams in MnBi_2Te_4 . *Phys. Rev. X* **11**, 011003 (2021).
 34. Liu, C. *et al.* Magnetic-field-induced robust zero Hall plateau state in MnBi_2Te_4 Chern insulator. *Nat. Commun.* **12**, 4647 (2021).
 35. Lin, W. *et al.* Direct visualization of edge state in even-layer MnBi_2Te_4 at zero magnetic field. *ArXiv210510234 Cond-Mat* (2021).
 36. Gong, Y. *et al.* Experimental Realization of an Intrinsic Magnetic Topological Insulator. *Chin. Phys. Lett.* **36**, 076801 (2019).
 37. Zhao, Y.-F. *et al.* Even–Odd Layer-Dependent Anomalous Hall Effect in Topological Magnet MnBi_2Te_4 Thin Films. *Nano Lett.* **21**, 7691–7698 (2021).
 38. Tai, L. *et al.* Polarity-tunable anomalous Hall effect in magnetic topological insulator MnBi_2Te_4 . *ArXiv210309878 Cond-Mat* (2021).
 39. Aliev, Z. S. *et al.* Novel ternary layered manganese bismuth tellurides of the $\text{MnTe-Bi}_2\text{Te}_3$ system: Synthesis and crystal structure. *J. Alloys Compd.* **789**, 443–450 (2019).
 40. Cui, J. *et al.* Transport properties of thin flakes of the antiferromagnetic topological insulator MnBi_2Te_4 . *Phys. Rev. B* **99**, 155125 (2019).
 41. Zeugner, A. *et al.* Chemical Aspects of the Candidate Antiferromagnetic Topological Insulator MnBi_2Te_4 . *Chem. Mater.* **31**, 2795–2806 (2019).
 42. Tan, C. *et al.* Hard magnetic properties in nanoflake van der Waals Fe_3GeTe_2 . *Nat. Commun.* **9**, 1554 (2018).
 43. Deng, Y. *et al.* Gate-tunable room-temperature ferromagnetism in two-dimensional Fe_3GeTe_2 . *Nature* **563**, 94 (2018).
 44. Liu, C. *et al.* Distinct Quantum Anomalous Hall Ground States Induced by Magnetic Disorders. *Phys. Rev. X* **10**, 041063 (2020).
 45. Blöchl, P. E. Projector augmented-wave method. *Phys. Rev. B* **50**, 17953–17979 (1994).

46. Kresse, G. & Joubert, D. From ultrasoft pseudopotentials to the projector augmented-wave method. *Phys. Rev. B* **59**, 1758–1775 (1999).
47. Kresse, G. & Furthmüller, J. Efficiency of ab-initio total energy calculations for metals and semiconductors using a plane-wave basis set. *Comput. Mater. Sci.* **6**, 15–50 (1996).
48. Kresse, G. & Furthmüller, J. Efficient iterative schemes for ab initio total-energy calculations using a plane-wave basis set. *Phys. Rev. B* **54**, 11169–11186 (1996).
49. Perdew, J. P., Burke, K. & Ernzerhof, M. Generalized Gradient Approximation Made Simple. *Phys. Rev. Lett.* **77**, 3865–3868 (1996).
50. Liechtenstein, A. I., Anisimov, V. I. & Zaanen, J. Density-functional theory and strong interactions: Orbital ordering in Mott-Hubbard insulators. *Phys. Rev. B* **52**, R5467–R5470 (1995).
51. Marzari, N., Mostofi, A. A., Yates, J. R., Souza, I. & Vanderbilt, D. Maximally localized Wannier functions: Theory and applications. *Rev. Mod. Phys.* **84**, 1419–1475 (2012).
52. Mostofi, A. A. *et al.* An updated version of wannier90: A tool for obtaining maximally-localised Wannier functions. *Comput. Phys. Commun.* **185**, 2309–2310 (2014).

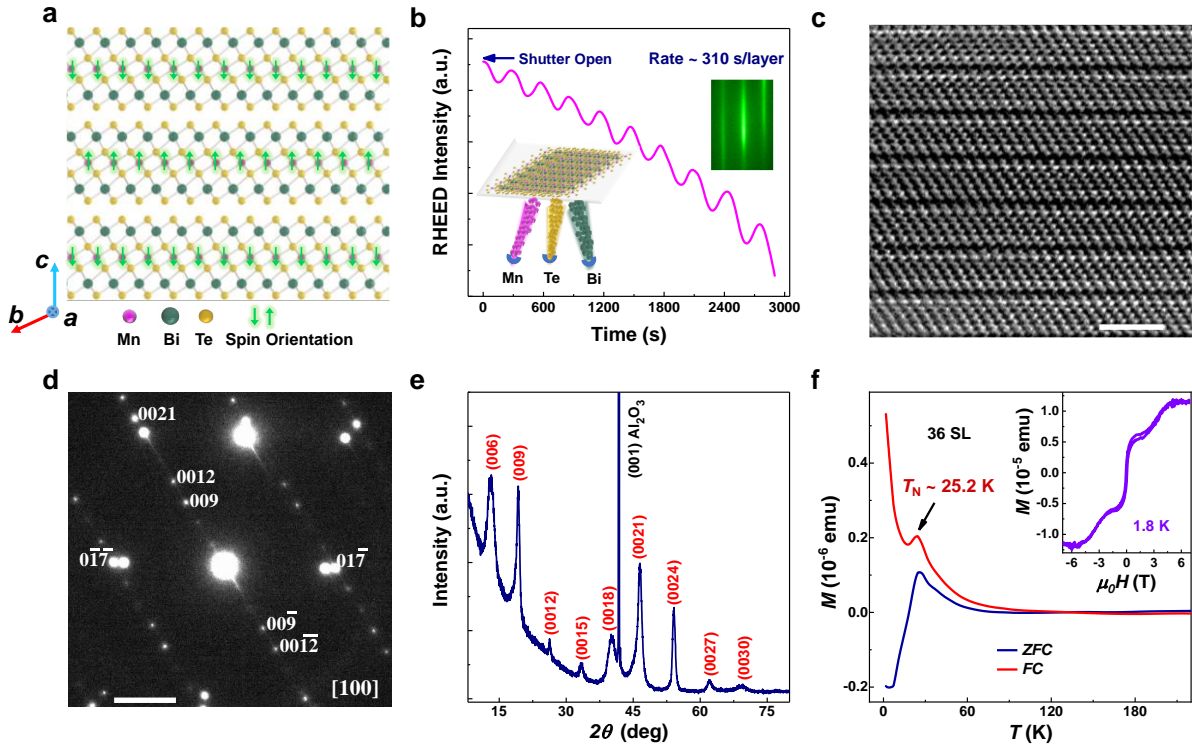


Figure 1 | Crystal structure and characterization of a 14 SL MnBi₂Te₄ film on (001) Al₂O₃ substrate. (a) Crystal structure of A-type AF MnBi₂Te₄ along the *a*-axis and the spins of Mn are marked with green arrows. (b) Layer-by-layer epitaxial mode observed from the RHEED oscillations. The left inset is a schematic illustration of the co-evaporation growth process of MnBi₂Te₄ films. The sharp RHEED pattern in the right inset suggests a smooth surface. (c) Cross-section HRTEM image along the *a*-axis. The scale bar is 2 nm. (d) Corresponding SAED pattern taken from [100] zone axis. The scale bar is 2 nm⁻¹. (e) The XRD spectrum, series of <003> peak showing the epitaxial orientation along *c*-axis. (f) ZFC-FC curves of magnetization as a function of temperature. Inset, Magnetization hysteresis of 36 SL MnBi₂Te₄ film at 1.8 K.

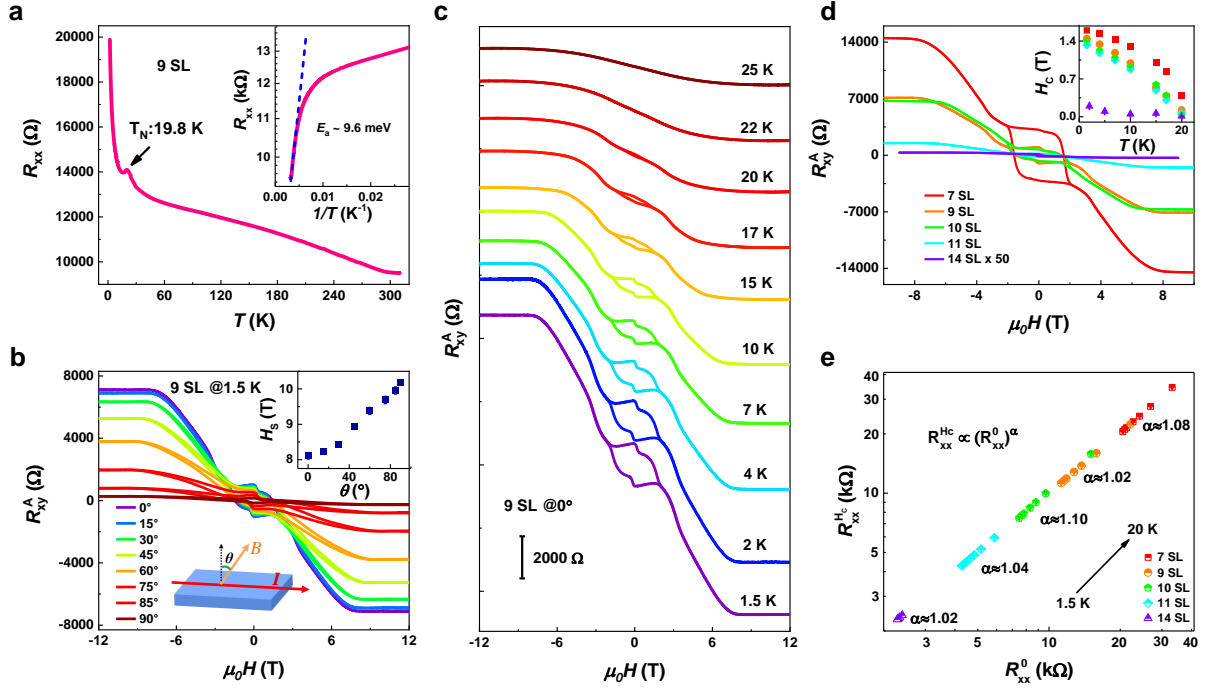


Figure 2 | Anomalous Hall insulator state in MnBi_2Te_4 films on Al_2O_3 substrate. (a) Temperature-dependence resistance R_{xx} . The kink point at 19.8 K corresponds to the magnetic transition temperature T_N . Inset is the fit to $R_{xx} \sim \exp(E_a/k_B T)$ with the excitation energy $E_a = 9.6$ meV. (b) Angle-dependent AHE curves. Schematic is the direction of the magnetic field with angle θ . Inset is the saturation magnetic field (H_s). (c) AHE curves versus temperature with $\theta = 0^\circ$. Inset shows the corresponding R_{xx} at 1.5 K. (d) Thickness-dependent AHE. With the thicknesses decreasing, the hysteresis becomes broader. Note that the lowest temperature of 14 SL film was 2 K and others were measured at 1.5 K. (e) Evolution of $R_{xx}^{H_C}$ versus R_{xx}^0 at different temperatures for 7 SL, 9 SL, 10 SL, 11 SL, 14 SL MnBi_2Te_4 samples.

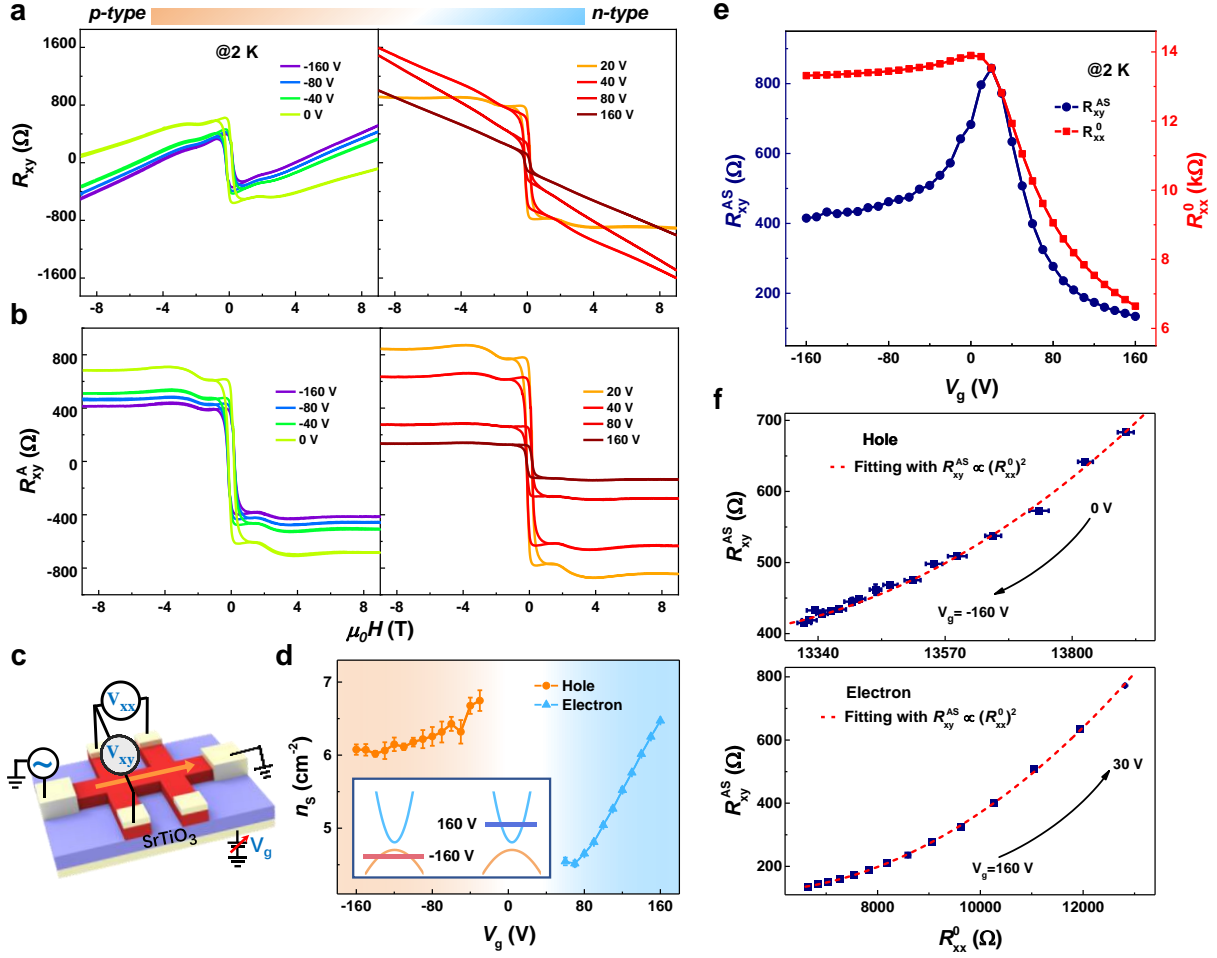


Figure 3 | Intrinsic Berry-curvature-dominated AHE of ~ 7 SL MnBi_2Te_4 on SrTiO_3 substrate. (a) Representative R_{xy} results under different gate voltages (V_g), with the n - p transition occurred at ~ 20 V. (b) The corresponding AHE results (R_{xy}^A) after linear subtraction from the normal Hall effect. Negative-sign AHE curves are preserved in both the electron- and hole-dominated regions. (c) Schematic diagram of six Hall-bar geometry under the gating effect. (d) Gate-dependent sheet carrier density (n_s). Inset, the Fermi level tuned from conduction band (blue line) to the valence band (orange line) as V_g changes from 160 V to -160 V. (e) Ambipolar R_{xy}^{AS} and R_{xx}^0 as a function of V_g . (f) R_{xy}^{AS} versus R_{xx}^0 in the hole-dominated and electron-dominated regions, the carmine dashed lines are the fits to the scaling law of $R_{xy}^{AS} \propto (R_{xx}^0)^2$. The preserved negative AHE curves in (b) and quadratic relation in (f) suggest that this AHE comes from the Berry curvature effect.

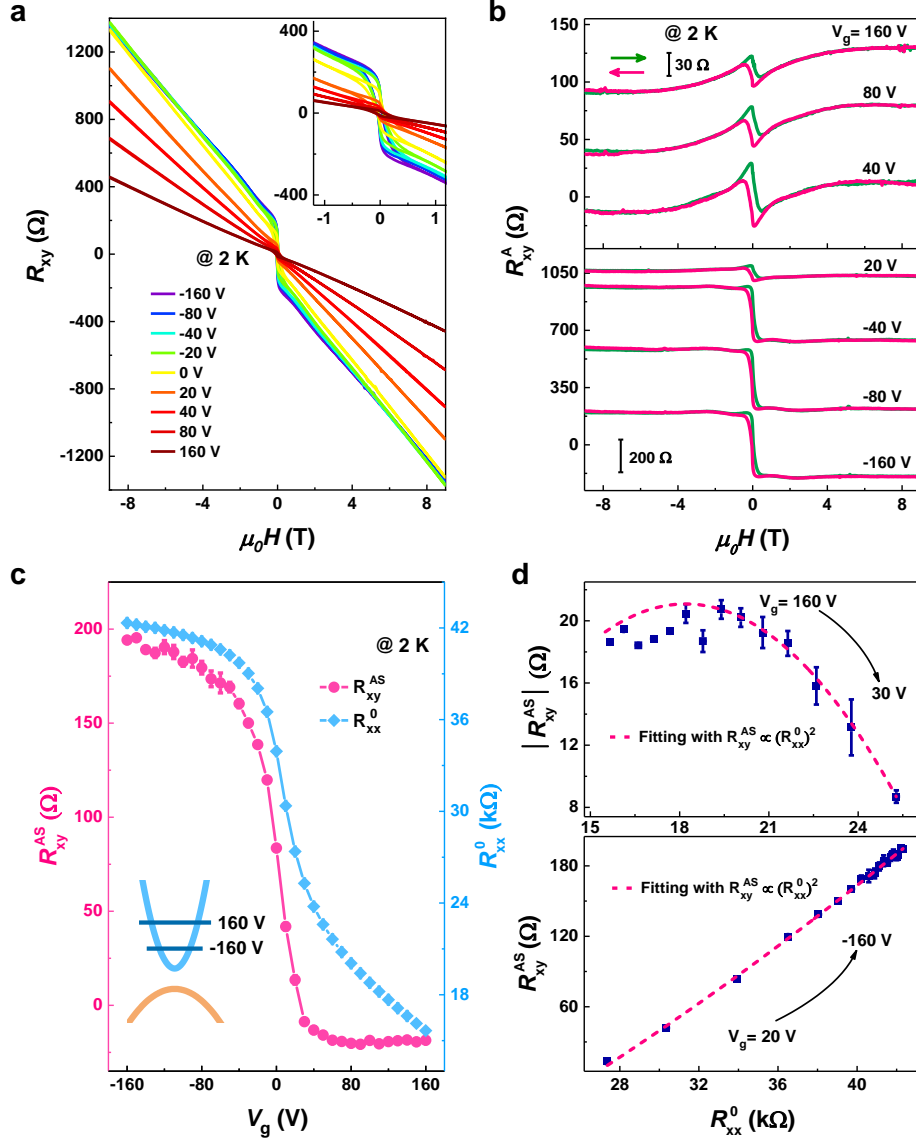


Figure 4 | AHE sign reversal in ~ 3 SL MnBi₂Te₄ on SrTiO₃ substrate. (a) Hall resistance under different gate voltages V_g , behaving n -type conduction in the whole gating range. Inset, the enlarged R_{xy} to show the hysteresis. (b) AHE curves after linear subtraction. The transition of AHE-sign appears at $V_g = 30$ V. (c) R_{xy}^{AS} and R_{xx}^0 versus V_g , both showing the monotonic trend. Inset, schematic diagram for the Fermi level modulation. (d) Quadratic scaling relation between R_{xy}^{AS} and R_{xx}^0 in the negative-sign and positive-sign AHE regions.

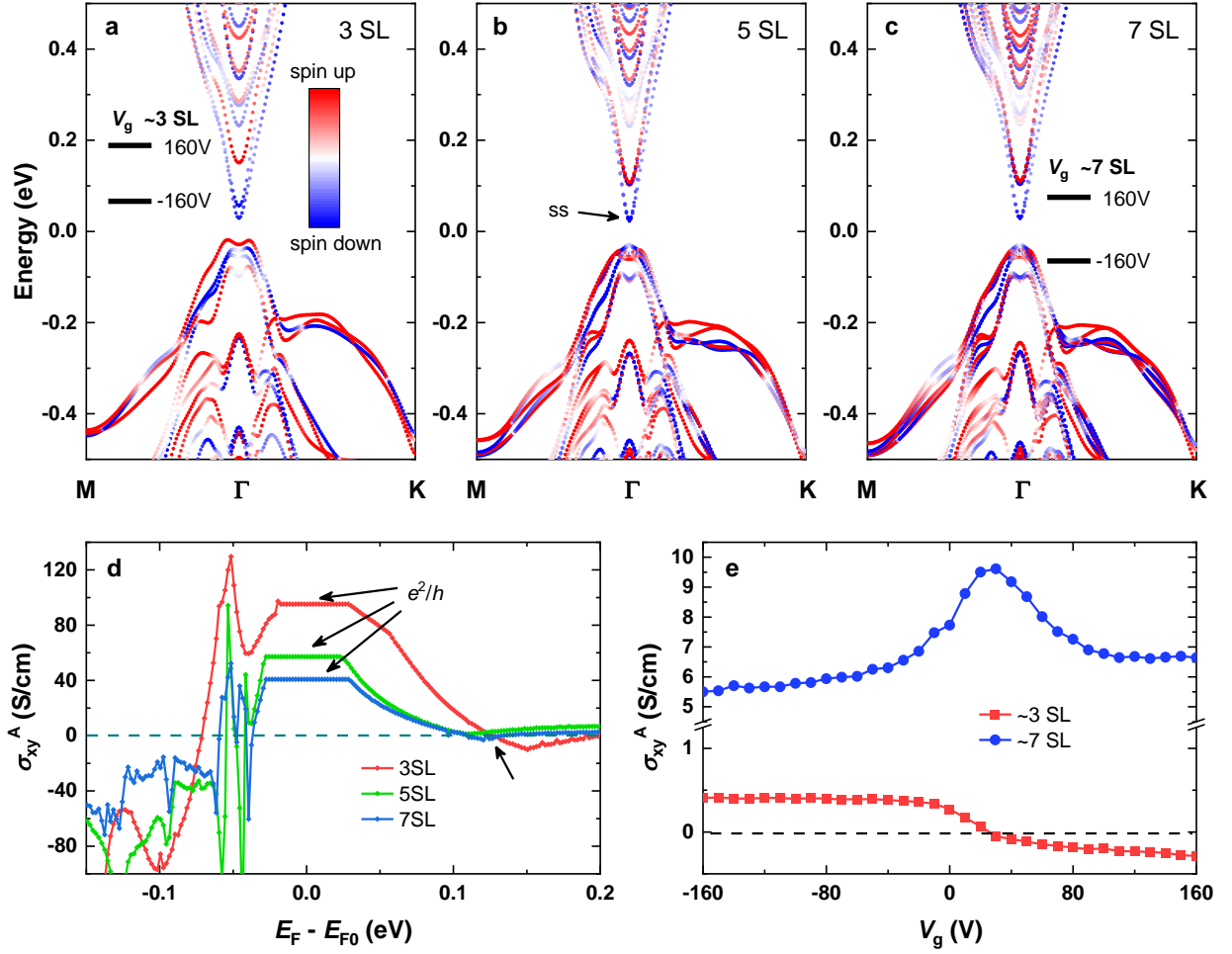


Figure 5 | Band structures and anomalous Hall conductivities (σ_{xy}^A) for odd-layered MnBi₂Te₄. (a)-(c) Spin-resolved band structure of 3 SL, 5 SL, and 7 SL MnBi₂Te₄. The Fermi energy is set to zero. In (b), the surface states (ss) are labeled for the first two conduction bands. In (a) and (c), the Fermi levels under various gate voltages V_g were deduced from magneto-transport results in Fig. 4 and Fig. 3, respectively. (d) Calculated σ_{xy}^A as a function of the Fermi energy. E_{F0} is the calculated intrinsic Fermi energy. Note that a transition of σ_{xy}^A from positive to negative appears around 0.12 eV for 3 SL. (e) Experimental σ_{xy}^A for ~ 3 SL and ~ 7 SL films as a function of gate voltage V_g .